VOL. 22, NO. 8, AUGUST 1985 J. AIRCRAFT 649

Propeller Aerodynamic Performance by Vortex-Lattice Method

Makoto Kobayakawa* and Hiroyuki Onuma†
Kyoto University, Kyoto, Japan

It is inappropriate to apply classical propeller theories to design an advanced turboprop (ATP). In this paper, the vortex-lattice method is applied to rotating blades. It is assumed that the flow is inviscid and incompressible. However, the compressibility effect is included in the calculations through the Prandtl-Glauert similarity rule. The other properties characteristics of an ATP, i.e., the effect of displacement velocities, the interference effect between blades, and the effect of flow deflection by a spinner and nacelle, are introduced into the calculations. Powers, thrusts, and efficiencies of two kinds of ATP, SR-1 and SR-3, are obtained and compared with experimental values. The numerical values show that they agree well with the experimental results of SR-1. However, the former is larger than those of SR-3. This is consistent with the calculations by Hamilton Standard. The principal reason for this difference is that the portion of the blade near the tip is distorted by centrifugal force. Using this method, the ATP performance can be calculated accurately below Mach 0.6. However, the transonic wing theory should be applied for performance estimates at Mach 0.7-0.8.

Nomenclature

a_0 = speed of sound
B = number of blades
C_P = power coefficient
C_T = thrust coefficient
D = diameter
F = influence coefficient, force component
f = blade surface
J = advance ratio
M = Mach number
m = number of panels
n = normal vector
N_S, N_C = number of divisions along spanwise and chordwise directions, respectively
P = power
Q = torque, strength of source
R = blade radius
T = thrust
u, v, w = velocity components
V, v = velocity vectors
V_∞ = flight speed
$\frac{1}{2} w$ = displacement velocity
x, y, z = coordinate axes on the blade, nondimensionalized by R
$\beta_{0.75R}$ = pitch angle at 75% radius
Γ = circulation
η = efficiency
Λ = swept angle
ρ = air density
ϕ = velocity potential
ω = circular frequency of propeller

Subscripts

C = control points
G = geometric velocity
I = induced velocity
i, j = ith and jth panels
k = kth blade

Superscript

$(\tilde{\ })$ = dimensional quantity

Introduction

THE advanced turboprop (ATP) is currently arousing great interest as a fuel-saving propulsion system for transport aircraft in the near future. ATP's are trying to improve efficiency from 15 to 30% at a cruise Mach number of 0.8 and from 25 to 40% at Mach 0.7 in comparison with turbofans. Therefore, ATP's are different from conventional turboprops in the following ways: ATP's have small diameters, many (8-10) thin and swept blades. Moreover, since the cruise speed is large, the effect of compressibility on the propeller performance becomes large. Accordingly, the classical theories[1,2] of propellers should give incorrect estimations for ATP's aerodynamics.

There exist many reports on ATP's, and the developments are quite advanced at NASA.[3-18] Sullivan[19] presented attractive results for swept blades using the vortex-lattice method (VLM). Recently, Hanson[20] applied the acceleration potential theory to the ATP. Jou[21] calculated the pressure distributions on the ATP blade surface in the transonic range by solving the perturbation velocity potential equation.

This paper presents the propeller performance calculations by the vortex-lattice method. For a rotating blade, the following principles are applied. First, a blade surface is divided into many trapezoidal panels, each panel represented by a helical horseshoe vortex. Second, induced velocities generated by all vortices on the control point of each panel are calculated by the Biot-Savart law. Boundary conditions on the blade surface are expressed so that the resultant velocities of geometric flow and induced flow take their direction along the surface, and the strength of the vortex in each panel is determined by these boundary conditions. Aerodynamic forces acting on the propeller blade are obtained by the Kutta-Joukowski theorem. Herein, incompressibility and nonviscosity are assumed throughout the flowfield. Although the vortex-lattice techniques are applied to the ATP, the following three effects, characteristic of an ATP, are taken into account here. First, the displacement velocity effect is introduced by following the classical propeller theory. Its effect is calculated by iteration. Second, the compressibility effect is calculated by the Prandtl-Glauert similarity rule. Finally, the effects of spinner and nacelle are introduced. Incoming flow to the blade is deflected by the propeller spinner and nacelle. We use the velocity distribution around an axisymmetric spinner and nacelle as the uniform flowfield to the blade.

As described above, the cruise Mach number of an ATP transport is 0.7-0.8; thus, the velocity of incoming flow to the blades is in the transonic range. Therefore, the aerodynamic performance of the blade is difficult to estimate by the VLM. However, the performance below Mach 0.6 can be

---

Received April 24, 1984; revision submitted Feb. 25, 1985.

*Associate Professor. Member AIAA.

†Graduate Student.

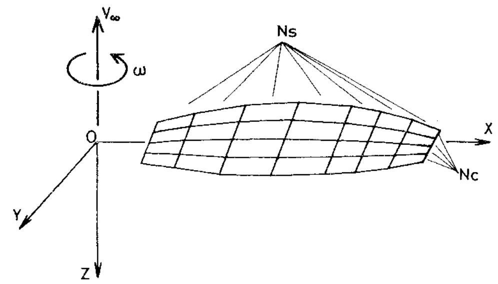

Fig. 1 Coordinate axes and blade division.

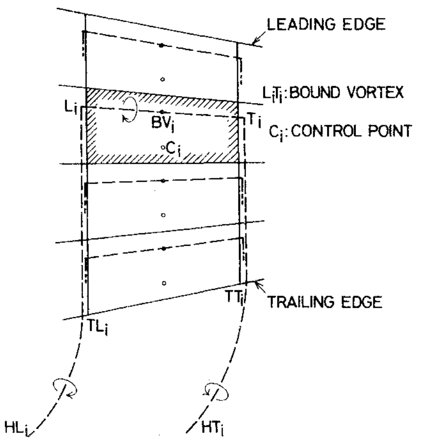

Fig. 2 Helical horseshoe vortex.

estimated accurately using this method and the force distributions over the blade can be calculated in detail. Moreover, the CPU times are shorter for these calculations. Accordingly, this method of calculation can be applied for the optimal design of an ATP blade.

Vortex-Lattice Method for Propellers

Propeller Geometry

The coordinate axes are fixed on the blade as illustrated in Fig. 1. To begin, the blade is divided into N_S spanwise sections by the lines perpendicular to the x axis which are intersections between the blade surface and the planes parallel with the yz plane. Then, the blade is divided into $N_S \times N_C$ trapezoidal panels by dividing the above sections into N_C parts along the chordwise direction and connecting these dividing points of all lines. As illustrated in Fig. 2, a bound vortex and a control point are put on the quarter chord line (L_iT_i) and the center of the three-quarter chord line (C_i) of each panel, respectively.

The wake vortices shed from both ends of the bound vortex proceed along the dividing lines until the trailing edge $(L_iTL_i$ and $T_iTT_i)$ is reached, and then depart from the blade surface growing as helical vortices $(TL_i\ HL_i$ and $TT_iHT_i)$ to infinity. The bound vortex and the two trailing helical vortices form a helical horseshoe vortex.

Induced Velocities

Since ATP's have more blades (8-10) than conventional propellers (2-4), the interference effects between the blades must be considered. Then, we give numbers to all of the blades as follows: Blade 0 is the blade under consideration, and blade k is the kth blade following blade 0 in the clockwise direction. Induced velocities generated by several vortices at the control point of the jth panel of blade 0 can be calculated using the Biot-Savart law in the same manner as Ref. 19. The following three velocities must be calculated.

1) Induced velocity by the bound vortices $(L_iT_i)_k$

$$\frac{v_{IBij}}{V_\infty} = \frac{\Gamma_i}{4\pi R V_\infty}[F_{uBij}F_{vBij}F_{wBij}]^T \tag{1}$$

where F_{uBij}, F_{vBij}, and F_{wBij} are influence coefficients which are the sums of influence coefficients from all blades, since the circulation of the ith bound vortex Γ_i is the same for all blades and, therefore, independent of k. Then, the influence coefficients are expressed as

$$F_{uBij} = \sum_{l}^{B} uBijl \text{ etc.} \tag{2}$$

2) Induced velocities by vortices $(L_iTL_i)_k$ and $(T_iTT_i)_k$

$$\frac{v_{ILij}}{V_\infty} = \frac{\Gamma_i}{4\pi R V_\infty}[F_{uLij}\ F_{vLij}\ F_{wLij}]^T \tag{3a}$$

$$\frac{v_{ITij}}{V_\infty} = \frac{\Gamma_i}{4\pi R V_\infty}[F_{uTij}\ F_{vTij}\ F_{wTij}]^T \tag{3b}$$

3) Induced velocities by helical trailing vortices started from $(TT_i)_k$ and $(TL_i)_k$

$$\frac{v_{IHLij}}{V_\infty} = \frac{\Gamma_i}{4\pi R V_\infty}[F_{uHLij}\ F_{vHLij}\ F_{wHLij}]^T \tag{4a}$$

$$\frac{v_{IHTij}}{V_\infty} = \frac{\Gamma_i}{4\pi R V_\infty}[F_{uHTij}\ F_{vHTij}\ F_{wHTij}]^T \tag{4b}$$

The induced velocity at C_i is the sum of the above velocities.

$$\frac{v_{ij}}{V_\infty} = \frac{v_{IBij} + v_{ILij} + v_{ITij} + v_{IHij} + v_{IHTij}}{v_\infty} = \frac{\Gamma_i}{4\pi R V_\infty}[F_{uij}\ F_{vij}\ F_{wij}]^T \tag{5}$$

where

$$F_{uij} = F_{uBij} + F_{uLij} + F_{uTij} + F_{uHLij} + F_{uHTij} \text{ etc.} \tag{6}$$

The induced velocity generated by all vortices is expressed by

$$\frac{v_{ij}}{V_\infty} = \left[\frac{u_{Ij}}{V_\infty}\ \frac{v_{Ij}}{V_\infty}\ \frac{w_{Ij}}{V_\infty}\right]^T = \left[\sum_i^m \frac{\Gamma_i}{4\pi R V_\infty}F_{uij} \sum_i^m \frac{\Gamma_i}{4\pi R V_\infty}F_{vij} \sum_i^m \frac{\Gamma_i}{4\pi R V_\infty}F_{wij}\right]^T \tag{7}$$

Furthermore, the velocity at C_j is

$$\frac{V_{Cj}}{V_\infty} = \frac{v_{Ij} + v_{Gj}}{V_\infty} = \left[\sum_i^m \frac{\Gamma_i}{4\pi R V_\infty}F_{uij} - \frac{\pi}{J}r_{Cj}\sin\gamma_{Cj}\quad \sum_i^m \frac{\Gamma_i}{4\pi R V_\infty}F_{vij} + \frac{\pi}{J}r_{Cj}\cos\gamma_{Cj}\quad \sum_i^m \frac{\Gamma_i}{4\pi R V_\infty}F_{wij} + 1\right]^T \tag{8}$$

where v_{Gj} is the resultant velocity ("geometric velocity") of the flight speed V_∞ and the rotating speed of the propeller $r\omega$ (r is nondimensionalized by R), and J is the advance ratio $\pi V_\infty / \omega R$.

Boundary Conditions

Boundary conditions at the control point on the blade surface are expressed by the tangency condition of the flow on the surface as follows:

$$V_{Cj} \cdot n_{Cj} = 0 \tag{9}$$

where n_{Cj} is a vector normal to the blade surface at the control point. If the blade surface is expressed by

$$z = f(x,y) \tag{10}$$

the boundary condition [Eq. (9)] is expanded as follows:

$$\left(\sum_i^m \frac{\Gamma_i}{4\pi R V_\infty} F_{uij} - \frac{\pi}{J} r_{Cj} \sin\gamma_{Cj}\right)\left(\frac{\partial f}{\partial x}\right)_{Cj} + \left(\sum_i^m \frac{\Gamma_i}{4\pi R V_\infty} F_{vij} + \frac{\pi}{J} r_{Cj} \cos\gamma_{Cj}\right)\left(\frac{\partial f}{\partial y}\right)_{Cj} = \sum_i^m \frac{\Gamma_i}{4\pi R V_\infty} F_{wij} + 1 \tag{11}$$

where the normal vector is written by

$$n_{Cj} = \text{grad}\,\{z - f(x,y)\}_{Cj} = \left[-\left(\frac{\partial f}{\partial x}\right)_{Cj}, -\left(\frac{\partial f}{\partial y}\right)_{Cj}, 1\right]^T \tag{12}$$

and x, y, and z are nondimensionalized by R.

Circulation Distribution and Forces Acting on the Propeller

Rewriting the boundary condition [Eq. (11)], we have

$$\sum_i^m A_{ji} \frac{\Gamma_i}{4\pi R V_\infty} = B_j, \qquad j = 1,2,\ldots,m \tag{13}$$

where

$$A_{ji} = F_{uij}\left(\frac{\partial f}{\partial x}\right)_{Cj} + F_{vij}\left(\frac{\partial f}{\partial y}\right)_{Cj} - F_{wij}$$

$$B_j = \frac{\pi}{J} r_{Cj}\left\{\sin\gamma_{Cj}\left(\frac{\partial f}{\partial x}\right)_{Cj} - \cos\gamma_{Cj}\left(\frac{\partial f}{\partial y}\right)_{Cj}\right\} + 1 \tag{14}$$

The above equations are a set of simultaneous linear equations with $\Gamma_i/4\pi R V_\infty$ unknowns. We can obtain the circulation distributions of the blade by solving these equations, and calculate the forces acting on the bound vortices by the Kutta-Joukowski theorem as follows:

$$F_i = \rho V_{BVi} \times \Gamma_i \overrightarrow{L_i T_i} \tag{15}$$

where ρ is air density and V_{BVi} the resultant velocity at BV_i, the center of the bound vortex L_iT_i.

We can also calculate thrust, torque, and power per blade by summing the thrust, torque, and power components over all of the panels. Therefore, the overall thrust, torque, and power of the propeller are given by

$$T = -B\sum_i^m F_{zi}$$

$$Q = B\sum_i^m (F_{yi}\cos\gamma_{BVi} - F_{xi}\sin\gamma_{BVi})\tilde{r}_{BVi}$$

$$P = Q\omega \tag{16}$$

The thrust and power coefficients and efficiency are defined as nondimensional parameters of the propeller as follows:

$$C_T = \frac{T}{\rho n^2 D^3}, \quad C_P = \frac{P}{\rho n^3 D^5}, \quad \eta = \frac{TV_\infty}{P} = J\frac{C_T}{C_P} \tag{17}$$

where $D = 2R$ and $n = \omega/2\pi$.

Some Effects of the Flowfield on the Propeller

Displacement Velocity

Coordinates of a helical horseshoe vortex shed from point TT_i on the trailing edge are expressed as follows:

$$x = \rho_{Ti}\cos\theta, \quad y = \rho_{Ti}\sin\theta, \quad z = \frac{V_\infty}{\omega R}(\theta - \theta_{Ti}) + z_{TTi} \tag{18}$$

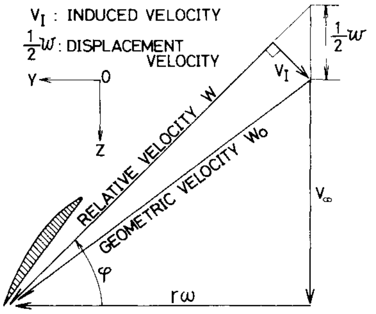

Fig. 3 Displacement velocity.

where ρ_{Ti} is the radius of the helical vortex (see Fig. 2), and θ the angle of an arbitrary point on the vortex from the x axis. Equation (18) neglects the effect of induced velocities by helical vortices. However, flow velocity increases after passing the propeller, and, moreover, the fluid begins a rotating motion. Therefore, the "displacement velocity" consideration in the classical propeller theory for this case should be applied as

$$x = \rho_{Ti}\cos\theta, \qquad y = \rho_{Ti}\sin\theta$$

$$z = \frac{V_\infty + \frac{1}{2} w_{Ti}}{\omega V_\infty}(\theta - \theta_{Ti}) + z_{TTi} \tag{19}$$

where $\frac{1}{2} w_{Ti}$ is the displacement velocity and is unknown in this case. Seeing the velocity diagram at an arbitrary radius shown in Fig. 3, the resultant velocity W is the vector sum of W_0 and V_I. Then, the wake vortex is shed along the z axis and the shedding speed is $V_\infty + \frac{1}{2} w$. From Fig. 3,

$$\tan\phi = \frac{V_\infty + \frac{1}{2} w}{r\omega R} = \frac{V_\infty + V_I/\cos\phi}{r\omega R} \tag{20}$$

Equation (20) now can be rewritten as

$$\left[1 + \left(\frac{J}{\pi r}\right)^2\right]\cos^2\phi + 2\frac{V_I}{V_\infty}\left(\frac{J}{\pi r}\right)^2\cos\phi + \left[\left(\frac{J}{\pi r}\right)^2\left(\frac{V_I}{V_\infty}\right)^2 - 1\right] = 0 \tag{21}$$

Furthermore, by

$$\tfrac{1}{2} w = \frac{V_I}{\cos\phi} \tag{22}$$

the displacement velocity can be calculated by solving Eq. (21) and substituting the solution into Eq. (22). However, J cannot be obtained explicitly because the displacement velocity is included in Eq. (19). Here, we obtained these velocities by iteration.

Prandtl-Glauert Similarity Rule

As described in the Introduction, using this VLM, it is difficult to calculate the propeller performance at Mach 0.8 where the flowfield of the blades is in the transonic range. Shock waves may occur on the blade surface and, therefore, the aerodynamic characteristics have to be investigated by transonic wing theory. However, the compressibility effect below Mach 0.6 can be estimated to some extent by modifying the incompressible calculations using the Prandtl-Glauert similarity rule.

Since the angle between the bound vortex $l_i = L_iT_i$ of ith panel and the geometric velocity v_{GBVi} at the center of the vortex is $\pi/2 - \Lambda_i$, the following relation is derived:

$$v_{GBVi} \cdot l_i = |v_{GBVi}|\,|l_i|\cos(\pi/2 - \Lambda_i) \tag{23}$$

Then,

$$\Lambda_i = \sin^{-1}\left[\frac{v_{GBVi}\cdot l_i}{|v_{GBV_i}|\ |l_i|}\right] \tag{24}$$

where Λ_i is the swept angle. Consequently,

$$\mu_i = \sqrt{1-M_i^2\cos^2\Lambda_i} \tag{25}$$

where M_i is the local Mach number defined by $M_i = |v_{GBVi}|/a_0$, where a_0 is the speed of sound. Following the Prandtl-Glauert similarity rule, the length of the ith panel is extended to $1/\mu_i$ times the original length along the chordwise direction. Therefore, the total chord length is extended to $\Sigma_i(1/N_C\mu_i)$ times.

Flowfield Around Spinner and Nacelle

The uniform flowfield into the propeller, i.e., the flight speed, is deflected by the spinner and nacelle. In conventional propeller theory, however, its effect is neglected since the aspect ratio of the blade is large. We have to consider spinner and nacelle effects for the ATP, however. Almost all spinners and nacelles are axisymmetric for the ATP. Therefore, we can represent the spinner and nacelle by distributing the sources appropriately along the z axis. The velocity potential of the flow by sources Q_i, $i=1,2,\ldots,N$, and uniform flow V_∞ is expressed by

$$\phi = V_\infty z - \sum_i^m \frac{Q_i}{4\pi}\frac{1}{l_i} \tag{26}$$

where

$$l_i = \sqrt{r^2+(z-z_i)^2}, \qquad r=\sqrt{x^2+y^2} \tag{27}$$

If the shape of the spinner and nacelle is given, the boundary conditions on the surface become a set of simultaneous equations with Q_i as unknowns. The velocity field around the spinner and nacelle can be calculated by

$$\begin{aligned} v_z &= \frac{\partial\phi}{\partial z} = V_\infty + \sum_i^N \frac{Q_i}{4\pi}\ \frac{z-z_i}{[r^2+(z-z_i)^2]^{3/2}} \\ v_r &= \frac{\partial\phi}{\partial r} = \sum_i^N \frac{Q_i}{4\pi}\ \frac{r}{[r^2+(z-z_i)^2]^{3/2}} \end{aligned} \tag{28}$$

Numerical Calculations and Discussions

In this section, the preceding methods will be applied to two kinds of ATP's, SR-1 and SR-3, that have been developed at Hamilton Standard, and the calculated results will be compared with the experimental values obtained at NASA. The blade shapes are illustrated in Fig. 4 wherein the dividing lines along the chordwise direction are shown. The blade surfaces are divided into $N_S \times N_C = 10\times 10 = 100$ for $SR=1$ and $12\times 10 = 120$ for SR = 3. An NACA 16-series airfoil is used for the blade cross sections. The following considerations are included in the calculations.

1) In the calculations of induced velocities, the upper bounds of numerical integration terminate at 4π (two revolutions) along the helical vortices because the flight speed for the ATP is large.

2) Induced velocities are calculated from all blades.

3) The drag force components are added to F_x, F_y, and F_z at the force calculation stage. The experimental values[22,23] of two-dimensional drag force acts on the blade along the incoming flow direction.

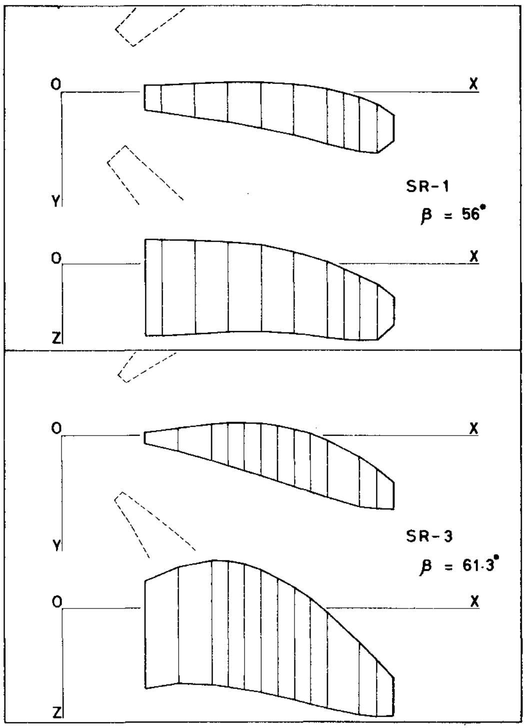

Fig. 4 Propeller configurations.

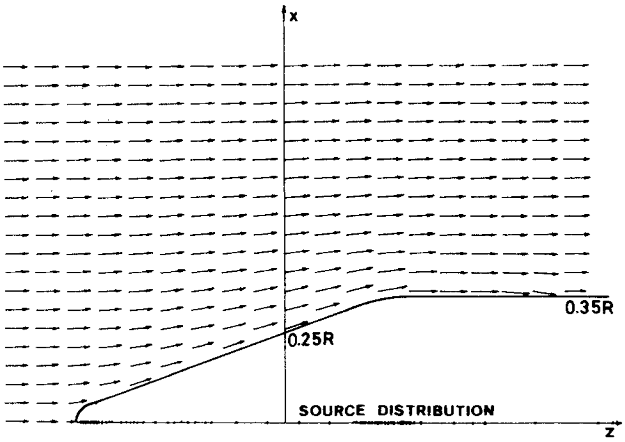

Fig. 5 Flow around spinner and nacelle.

4) In the displacement velocity calculations, the initial value is set at zero. The iteration converges approximately five times.[24]

5) The flight Mach number is taken to be 0.6 (constant) for all cases. The Prandtl-Glauert similarity rule is applied for this Mach number.

6) For the spinner and nacelle calculations, a simple configuration is used, as shown in Fig. 5. The flowfield around the spinner and nacelle and the source distribution are illustrated in Fig. 5 as well.

The pitch angles at 75% radius, $\beta_{0.75R}$, are taken as 54, 56, and 58 deg for SR-1, and 59.3, 61.3, and 63.3 deg for SR-3. The circulation distributions of SR-3 ($\beta_{0.75R} = 61.3$ deg, $J=3$) are shown in Fig. 6. The outer figure illustrates the spanwise distribution and the inner figure shows the chordwise distributions at 40, 77.5, and 97.5% of the blade radius. Efficiencies (η) and power coefficients (C_P) of SR-1 and SR-3 are compared with the experimental values and are shown in Figs. 7 and 8, respectively. The numerical results of SR-1 agree well with the experimental values. However, for the case of SR-3, the numerical results of C_P are larger than of the experimental results. On the other hand, the numerical results of η agree

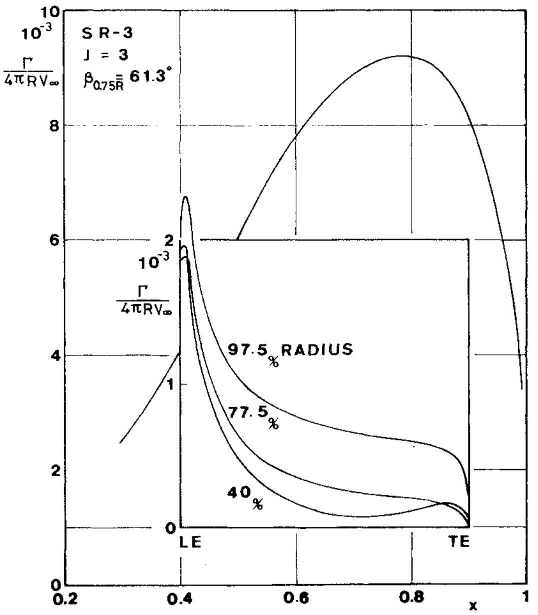

Fig. 6 Circulation distributions of SR-3.

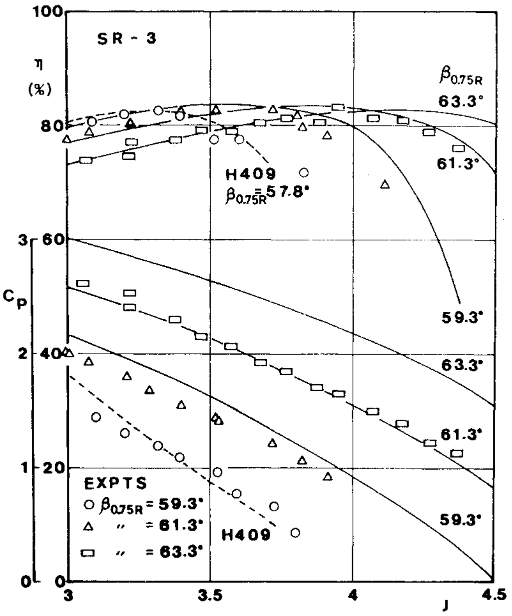

Fig. 8 Power coefficients and efficiencies of SR-3.

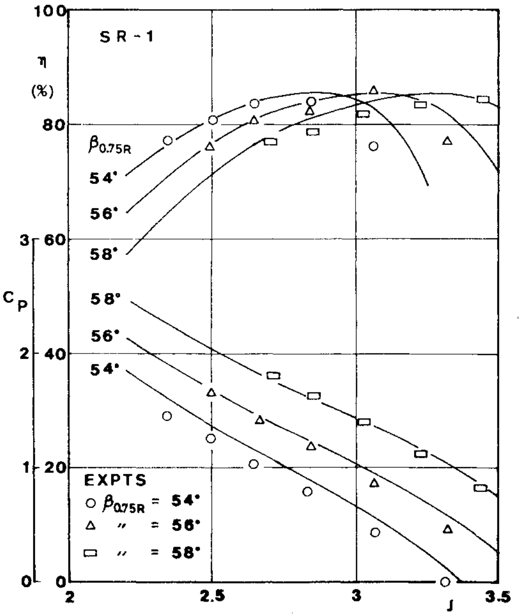

Fig. 7 Power coefficients and efficiencies of SR-1.

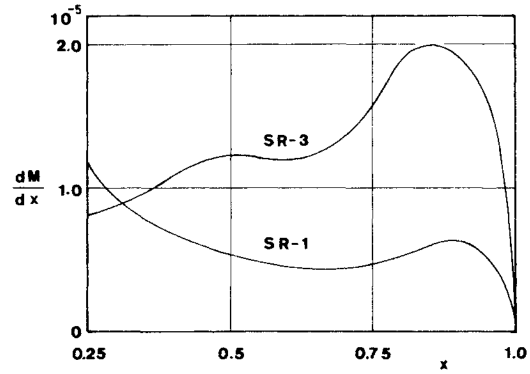

Fig. 9 Torsional moment distributions.

well with those of experiments for small J, but become larger when J becomes large. Looking at this figure carefully, the numerical results of C_P agree with the experimental results for the case of $\beta_{0.75R}$ two deg smaller. In Fig. 8, the calculated results by Hamilton Standard (H409) are also illustrated, where $\beta_{0.75R}$ is 57.8 deg. Noticing the fact that $\beta_{0.75R}$ of H409 is less than $\beta_{0.75R}$ of this case (59.3 deg) for 1.5 deg, it may be considered that the results are consistent with each other.

The main reason for the differences between the experimental values and the calculations might be centrifugal force, i.e., the blade portion near the tip is distorted by centrifugal force. The torsional moment distributions acting on the blades from centrifugal force are shown in Fig. 9. By this figure, it is clear that the moment generated on SR-3 is larger than on SR-1. Especially the moment level on SR-3 where the peak is near $0.85R$. The torsional moment by aerodynamic forces should also be considered as the reason of the reduced pitch angle, however, that is very small.

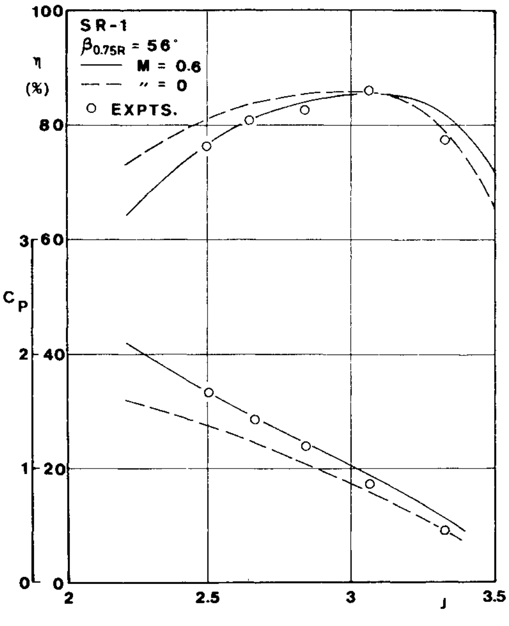

Fig. 10 Compressibility effect on SR-1.

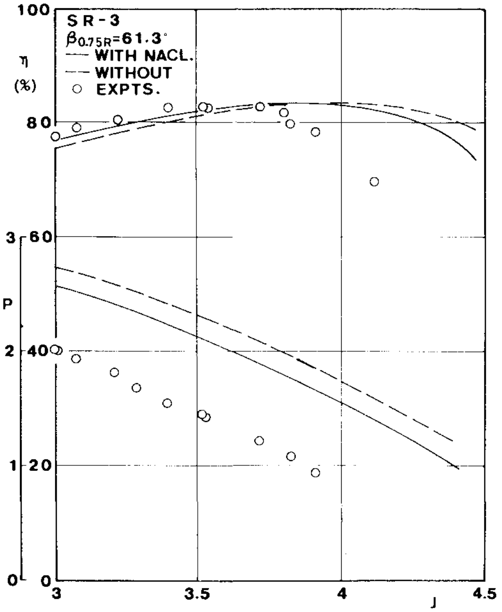

Fig. 11 Flow deflection effect on SR-3.

Finally, in Figs. 10 and 11, the effects of the Prandtl-Glauert similarity rule and flow deflection by the spinner and nacelle are shown. The results including these effects become closer to the experimental values than those without these effects.

Conclusions

It is inappropriate to apply the classical propeller theory to design on advanced turboprop (ATP). Several methods and techniques are developed to estimate the aerodynamic performances of an ATP. In this paper, the vortex-lattice method is applied to rotating blades. In particular, the following points for rotating blades of ATP are taken into account: 1) displacement velocities, 2) the Prandtl-Glauert similarity rule, 3) interference effects between blades, and 4) flow deflection by the spinner and nacelle.

Numerical calculations are performed for two kinds of ATP—SR-1 and SR-3—developed at Hamilton Standard, and are compared with experimental values obtained at NASA. The results of calculations show that the numerical values for SR-1 agree well with the experimental values. However, for SR-3, the former is larger than the latter. This fact is consistent with the calculations by Hamilton Standard. The principal reason for these differences is that the blades are distorted by centrifugal force.

Acknowledgments

The authors express their thanks to Messrs. Akira Ohara and Yoshifumi Kawakami of Sumitomo Precision Products for helpful discussions throughout this research.

References

[1] Goldstein, S., "On the Vortex Theory of Screw Propeller," *Proceedings of the Royal Society of London,* Ser. A23, 1929, pp. 440-465.

[2] Theodorsen, T., *Theory of Propellers,* McGraw-Hill Book Co., New York, 1948.

[3] Rohrbach, C. and Metzger, F. B., "The Prop-Fan—A New Look in Propulsors," AIAA Paper 75-1208, 1975.

[4] Rohrbach, C., "A Report on the Aerodynamic Design and Wind Tunnel Test of a Prop-Fan Model," AIAA Paper 76-667, 1976.

[5] Dugan, J. F. et al., "Advanced Turboprop Technology Development," AIAA Paper 77-1223, 1977.

[6] Black, D. M. et al., "Aerodynamic Design and Performance Testing of an Advanced 30° Swept Eight Bladed Propeller at Mach Numbers from 0.2 to 0.85," NASA CR 3047, 1978.

[7] Dugan, J. F. et al., "Prop-Fan Propulsion—Its Status and Potential," SAE TP 780995, 1978.

[8] Bober, L. T. and Mitchell, G. A., "Summary of Advanced Methods for Predicting High-Speed Propeller Performance," AIAA Paper 80-0225, 1980.

[9] Coussens, T. G. and Tullis, R. H., "Propfans; Propulsion Systems of Future?," *Automotive Engineering,* Vol. 88, No. 68, June 1980, pp. 65-69.

[10] Dugan, J. F. et al., "The NASA High-Speed Turboprop Program," SAE TP 801120, 1980.

[11] Nystrom, P. A. and Farassat, F., "A Numerical Technique for Calculation of the Noise of High-Speed Propellers with Advanced Blade Geometry," NASA TP 1662, 1980.

[12] Bober, L. J. and Chang, L. K., "Factors Influencing the Predicted Performance of Advanced Propeller Designs," NASA TM 82676, 1981.

[13] Serafini, J. S. et al., "Laser-Velocimeter Flow-Field Measurements of an Advanced Turbo-Prop," AIAA Paper 81-1568, 1981.

[14] Little, B. H. and Trimboli, W. S., "An Experimental Investigation of S-Duct Diffusers for High-Speed Prop-Fans," AIAA Paper 82-1120, 1982.

[15] Mackall, K. G. et al., "In Flight Acoustic Results from an Advanced-Design Propeller at Mach Numbers to 0.8," AIAA Paper 82-1123, 1982.

[16] Mitchell, G. A. and Mickelson, D. C., "Summary and Recent Results from the NASA Advanced High-Speed Propeller Research Program," AIAA Paper 82-1119, 1982.

[17] Rohrbach, C. et al., "Evaluation of Wind Tunnel Performance Testings of an Advanced 45° Swept Eight-Bladed Propeller at Mach Number from 0.45 to 0.85," NASA CR 3505, 1982.

[18] Strack, W. C. et. al., "Technology and Benefits of Aircraft Counter Rotation Propellers," NASA TM 82983, 1982.

[19] Sullivan, J. P., "The Effect of Blade Sweep on Propeller Performance," AIAA Paper 77-716, 1977.

[20] Hanson, D. B., "Compressible Helicoidal Surface Theory for Propeller Aerodynamics and Noise," *AIAA Journal,* Vol. 21, June 1983, pp. 881-889.

[21] Jou, W. H., "Finite Volume Calculation of Three-Dimensional Potential Flow Around a Propeller," *AIAA Journal*, Vol. 21, Oct. 1983, pp. 1360-1364.

[22] Borst, H. V. et al., "Summary of Propeller Design Procedures and Data," Vols. I-III, USAAMRDL TR 73-34C, 1973.

[23] Lindsey, W. F. et al., "Aerodynamic Characteristics of 24 NACA 16-Series Airfoils at Mach Numbers Between 0.3 and 0.8," NACA TN 1546, 1948.

[24] Nishida, M., "The Effect of Displacement Velocity on Propeller Performance," *Journal of Aircraft,* Vol. 20, Aug. 1983, pp. 734-736.